

## Shear velocity structure of the Mariana mantle wedge from Rayleigh wave phase velocities

Moira L. Pyle,<sup>1,2</sup> Douglas A. Wiens,<sup>1</sup> Dayanthie S. Weeraratne,<sup>3</sup> Patrick J. Shore,<sup>1</sup> Hajime Shiobara,<sup>4</sup> and Hiroko Sugioka<sup>5</sup>

Received 15 September 2009; revised 7 June 2010; accepted 18 June 2010; published 6 November 2010.

[1] We examine the seismic structure of the Mariana mantle wedge using data from a combined deployment of ocean bottom seismographs and land stations in 2003–2004. We measure Rayleigh wave phase velocities and invert these results for the shear velocity structure and azimuthal anisotropy in the region. In the back-arc region low phase velocities indicate shear velocities as low as  $3.9 \pm 0.1$  km/s at depths of about 60 km. Locations of the lowest seismic velocities at 18.0°N–18.5°N, 16.0°N–16.5°N, and 14.0°N–14.5°N correspond to the locations of gravity lows and probably indicate the presence of temperature and melt production maxima compared to elsewhere along the spreading center. The shape of the low velocity anomaly also indicates that there is a degree of asymmetry to the thermal structure across the spreading center. The fore arc exhibits low shear velocities ( $V_s \sim 3.6$  km/s) at depths shallower than 40 km. These low uppermost mantle velocities are likely due to serpentization of the fore arc. Azimuthal anisotropy results suggest an average peak-to-peak anisotropy of about 1%–2% with a fast direction of NNE. Fore-arc anisotropy shows arc-parallel fast directions at shallow depth in agreement with previous shear wave splitting observations and deeper arc-perpendicular directions influenced by the slab. Back-arc anisotropy is largely arc perpendicular, consistent with splitting observations west of the spreading center.

**Citation:** Pyle, M. L., D. A. Wiens, D. S. Weeraratne, P. J. Shore, H. Shiobara, and H. Sugioka (2010), Shear velocity structure of the Mariana mantle wedge from Rayleigh wave phase velocities, *J. Geophys. Res.*, *115*, B11304, doi:10.1029/2009JB006976.

### 1. Introduction

[2] The mantle wedge is an area of intensive geological, geophysical, and geochemical study. Investigation of the processes and structure in this region is essential for an understanding of the dynamics of plate tectonics. Among the many questions that exist about the mantle wedge are those concerning the location and depth extent of melt beneath island arcs and back-arc spreading centers and the direction and nature of mantle flow. The study of seismic velocities, anisotropy, and attenuation is a crucial component of these investigations because these measurements provide insight about many key unknowns in mantle structure such as the temperature, water content, presence of melt, composition, mantle flow patterns, and deformation styles (a discussion of

the relationship of seismic observables to these physical properties is given by *Wiens et al.* [2006, 2008]). Most of the information we have about seismic velocities in the mantle wedge comes from body wave tomography. High-resolution tomography images significant low velocity anomalies beneath the volcanic front and above the slab in several subduction zones [e.g., *Husen et al.*, 2003; *Reyners*, 2006; *Wagner et al.*, 2005; *Zhao et al.*, 1994, 1997]. Tomography from the Lau region shows a large low velocity anomaly between 40 and 100 km depth beneath the back-arc spreading center [*Zhao et al.*, 1997]. The direction of mantle flow is usually inferred from shear wave splitting results, which can vary widely in different subduction zone environments. In the Mariana and Tonga subduction zones, complex mantle flow is suggested by fast splitting directions which are parallel near the volcanic arc and rotate to the direction of convergence in the back arc [*Pozgay et al.*, 2007; *Smith et al.*, 2001]. Few surface wave studies of subduction zones exist, but their analysis can provide additional constraints on the shear velocity structure and azimuthal anisotropy within the mantle wedge.

[3] The Mariana subduction zone offers an excellent setting to examine the workings of the mantle wedge because it includes a wide variety of tectonic features, including an active back-arc spreading center, and the marine environ-

<sup>1</sup>Department of Earth and Planetary Sciences, Washington University in St. Louis, St. Louis, Missouri, USA.

<sup>2</sup>Now at Department of Geology and Geophysics, University of Utah, Salt Lake City, Utah, USA.

<sup>3</sup>Department of Geological Sciences, California State University, Northridge, California, USA.

<sup>4</sup>Earthquake Research Institute, University of Tokyo, Tokyo, Japan.

<sup>5</sup>Institute for Frontier Research on Earth Evolution, JAMSTEC, Yokosuka, Japan.

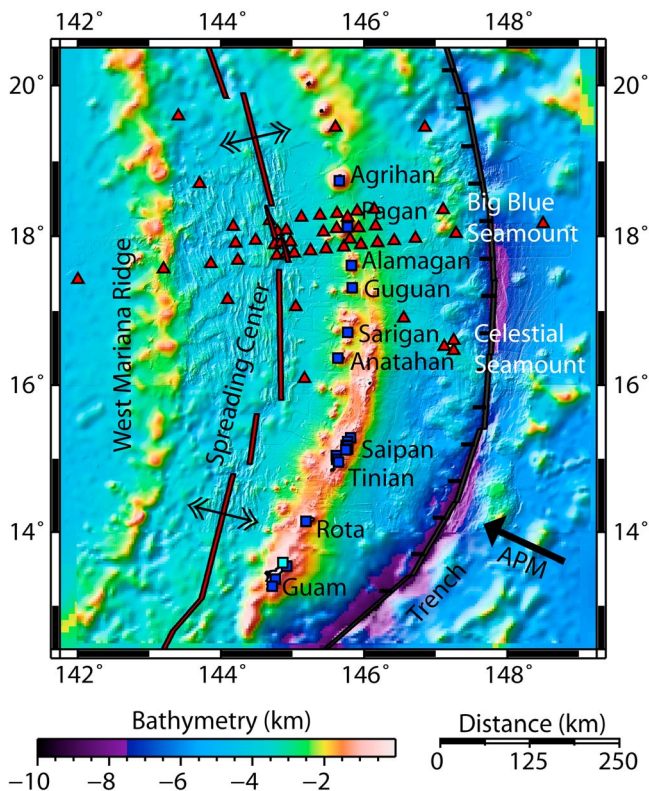


**Figure 1.** Map of the study area. Gray (red) triangles mark locations of OBS stations which returned data, and white (blue) squares mark locations of land stations. The light gray (light blue) square marks the location of the GSN station GUMO. The location of the trench is indicated by the hatched black line, and the locations of the back-arc spreading segments are indicated by the solid black (dark red) lines. The direction of spreading is perpendicular to the lines as indicated by the double arrows. The solid black arrow indicates the direction of absolute plate motion for the Pacific plate. Names of seamounts mentioned in the text and some islands are shown.

ment also has the advantage of avoiding contamination from the continental crust. Along the arcuate trench, the Pacific plate subducts beneath the Philippine Sea plate in a northwesterly direction (Figure 1) producing nearly strike-slip convergence in the north varying to almost orthogonal convergence in the southern part of our study area with typical trench axis depths of 6–8 km [McCaffrey, 1996; Stern *et al.*, 2003]. Seismicity shows that the slab is nearly vertical in our study area [Engdahl *et al.*, 1998], and no slab rollback is observed [Stern *et al.*, 2003]. Active serpentinite mud volcanoes are observed near the trench indicating serpentinization of the fore arc [Fryer, 1996; Fryer *et al.*, 1999]. The active volcanic arc is mostly submarine south of Anatahan [Bloomer *et al.*, 1989; Meijer, 1982]. The arc is separated from a remnant island arc (the West Mariana Ridge) by the back-arc spreading center. The central portion of the trough began spreading around 6 Ma with a spreading half rate around 2 cm/yr [Iwamoto *et al.*, 2002].

[4] In this paper, we examine Rayleigh wave phase velocities recorded by a recent deployment of seismographs located on islands and on the ocean bottom to study the

mantle wedge in the Mariana arc system. Rayleigh waves are primarily sensitive to the shear velocity structure. Body wave tomography can often generate excellent lateral resolution, but in the upper mantle where the raypaths are largely vertical, velocity anomalies may be smeared vertically. Surface waves have improved depth resolution due to their dispersive properties and so provide important and independent constraints on the depth and location of shear velocity anomalies in the oceanic mantle. In addition, shear wave structure can be difficult to obtain from body waves due to high attenuation of *S* wave arrivals in subduction zones and poor signal-to-noise ratio of horizontal components in ocean bottom seismometers at the base of the water column. Complex structure along the raypath, which may produce deviations from the great circle path, multipathing, and scattering, can also present problems for surface wave studies. Recent developments in surface wave analysis provide a simple but effective way of dealing with most of these complications by modeling the incoming wave as the sum of two interfering plane waves [Forsyth and Li, 2005]. We use this new method to investigate Rayleigh wave phase velocities and their corresponding shear velocities in the Marianas to image low velocity regions beneath the volcanic arc and back-arc spreading center. We also examine azimuthal anisotropy of the Rayleigh waves in order to study mantle flow within the wedge.

## 2. Data Selection and Processing

[5] We use data obtained during the Multi-Scale Seismic Imaging of the Mariana Subduction Factory experiment. This project was a joint U.S.–Japanese collaborative effort including multichannel seismic reflection, controlled source wide angle seismic reflection and refraction, and passive seismic recording. Our study utilizes data from the passive seismic deployment of the experiment which includes 20 broadband land stations from the Program for Array Seismic Studies of the Continental Lithosphere (PASSCAL), 50 semibroadband ocean bottom seismographs (OBSs) from the U.S. National Ocean Bottom Seismograph Instrument Pool, and eight Japanese semibroadband OBSs. The instruments were deployed from June 2003 until May 2004. Land stations were located along the islands of the active volcanic arc, while the OBSs were densely dispersed around the island of Pagan and over the active back-arc spreading center and extended more sparsely from the West Mariana Ridge to the fore arc (Figure 1). Land stations used either Streckeisen STS-2 or Guralp CMG-40T sensors, but due to the close station spacing of the 40T sensors and the better long period recording of the STS-2s, we use only stations with the STS-2 sensors for this study. The U.S. OBSs were operated by Lamont Doherty Earth Observatory and used three-component Mark Products L4 sensors; 15 of the instruments had 16 bit data loggers and 35 of the instruments had a newer 24 bit design. The Japanese OBSs were built and operated by the University of Tokyo and used precision measuring device (PMD) (WB2023LP) sensors. Forty-nine of the OBSs were recovered and returned useful data. The 35 U.S. OBSs with the 24 bit design returned data for only approximately 50 days due to a firmware defect which limited the duration of the data recording. The remaining OBSs returned data for the entire duration

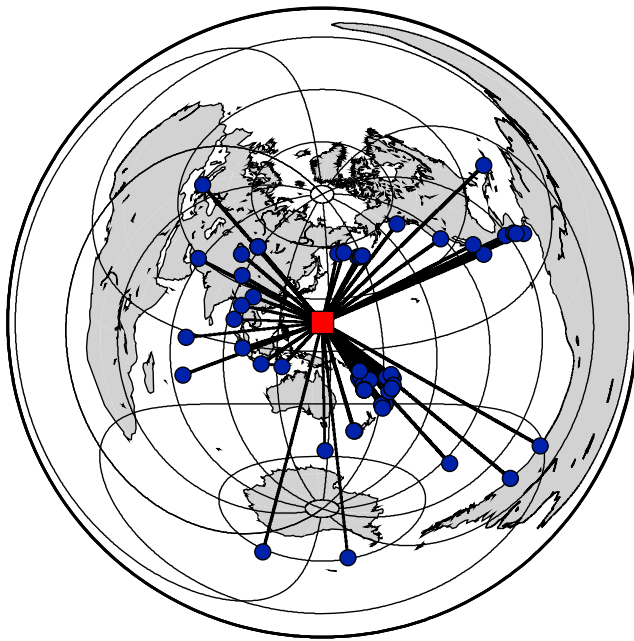


**Figure 2.** Location of earthquakes used in this study. Dark gray (blue) circles denote earthquakes, and the light gray (red) square marks the location of the study area. Connecting lines show great circle paths between events and the study area.

(11 months) of the experiment. In addition, we also use data from the Incorporated Research Institutions for Seismology/U.S. Geological Survey (IRIS/USGS) Global Seismographic Network (GSN) station GUMO located on the island of Guam. The locations of all land and ocean bottom seismographs that returned data are given by *Pozgay et al.* [2007].

[6] As a first step in the analysis, we examined all events occurring between  $30^\circ$  and  $150^\circ$  from the array with depths shallower than 200 km. Each event was visually inspected for a good signal-to-noise ratio (SNR) of the Rayleigh wave on the vertical trace at each frequency considered. Events with good waveforms at fewer than 10 stations were discarded because they generally lack enough information to be useful for the array analysis described in section 3. We found a total of 59 teleseismic events that recorded usable Rayleigh waves during the time of deployment. From these events, 37 show usable Rayleigh waves on the ocean bottom seismograph records at periods of 59 s or longer. The events range in magnitude from  $M_w$  6.0 to 7.8 and have a wide azimuthal distribution (Figure 2). The largest gap in the distribution occurs to the ESE of the study array in the direction of South America. Signal quality is generally best at periods of 29–40 s, and the greatest density of crossing paths is obtained at these periods (Figure 3). At periods below 20 s and for some events at 20–22 s, waveforms are either incoherent or demonstrate complex beating, likely due to long path distances through complicated crustal structures and sensitivity to the deep water column prior to arrival in the study region. At longer periods, starting at 55 s but particularly above 67 s, many of the smaller events exhibit a reduced SNR. Despite these limitations, raypath coverage is

sufficient to permit a well-constrained tomographic inversion for Rayleigh wave phase velocity at periods between 20 and 67 s, with the best resolution around the island of Pagan and the back-arc spreading center where instrumen-

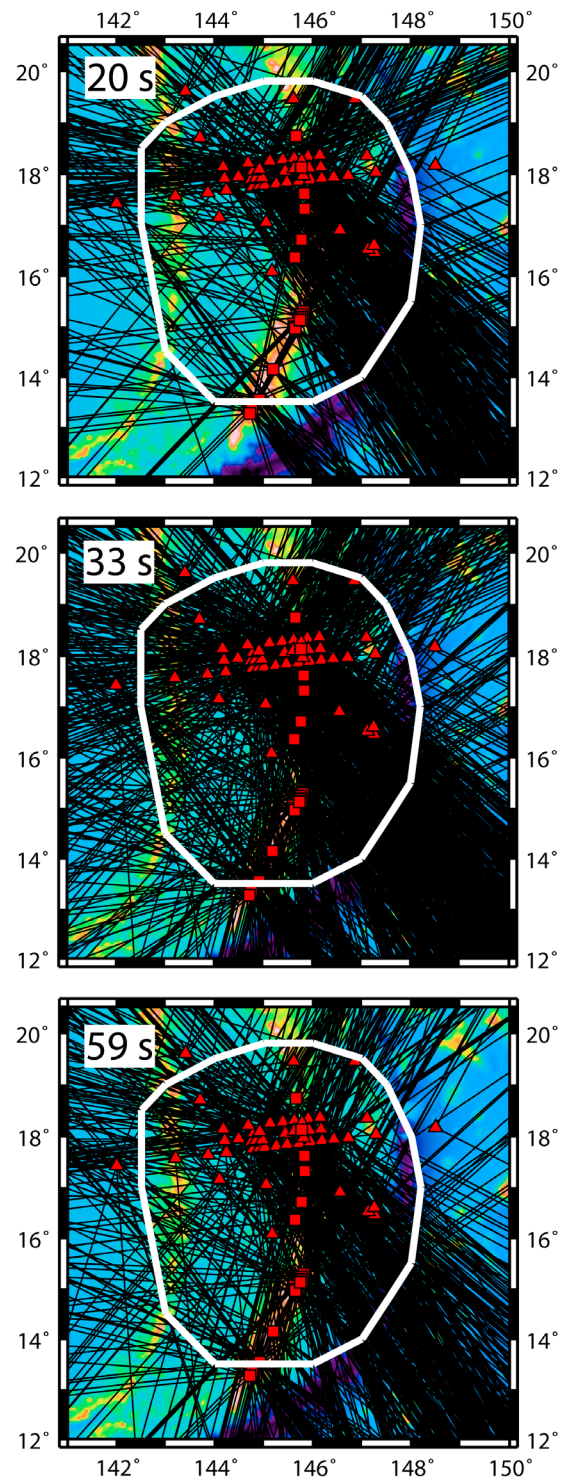


**Figure 3.** Raypath coverage for the 20, 33, and 59 s periods in our study area. White (red) triangles mark locations of OBS stations, and squares mark the locations of land stations. The light gray (white) polygons outline the areas of greatest resolution.

**Table 1.** Number of Events and Raypaths Used at Each Period

Period (s)	Number of Events	Number of Paths
20	30	831
22	52	1474
25	55	1569
29	57	1610
33	53	1500
40	49	1366
45	44	1184
50	41	1070
55	37	945
59	37	907
67	26	638

tation was the densest. Table 1 lists the number of events and raypaths used at each frequency.

[7] In order to compare Rayleigh wave phases and amplitudes from the different types of sensors used in this project, the instrument response was removed from each record. We tested the nominal OBS instrument response by comparing waveforms from the Lamont OBSs located around the island Pagan with the two STS-2 stations located on the island. The STS-2s have well-known instrument responses (including the gain), and the Pagan stations have a close enough proximity to the dense array of OBSs surrounding the island that the waveforms can be expected to be similar at long periods with a small time discrepancy due to different distances to the event. We chose a large event arriving with a back azimuth such that the waveforms had the same theoretical arrival time at both one of the land stations and one or more of the OBSs. We removed the instrument response to velocity using the poles and zeros from the raw Lamont OBS and land station records using a tapered filter which is flat between 1 and 250 s. The resulting velocity records were nearly identical, except for a difference in amplitude. The amplitude at several different frequency ranges was measured for both the land stations and the OBSs, and we found an average factor of difference between the two amplitudes as our correction for the gain factor. For the 16 bit OBSs, the correction is  $-1.75$ , and for the 24 bit instruments, the correction is  $-1.417$ . Only a constant correction was required because the difference in amplitudes was consistent over the different frequency bands.

[8] The instrument response for the Japanese OBSs was tested by comparing it with that of adjacent U.S. OBSs and land stations after the amplitude correction described above. After we removed the nominal instrument response provided by the manufacturer of the PMD sensor, we observed a systematic phase discrepancy between data recorded at Japanese OBSs and data recorded at adjacent U.S. stations. To compensate for this, we found an empirical correction for the Japanese OBS instrument response using spectral division. We first select an event recorded at a Japanese OBS and an adjacent U.S. OBS with theoretical Rayleigh wave arrival times within  $\sim 5$  s of each other and good SNR between 15 and 100 s. The U.S. OBS recording is shifted in time to match the theoretical arrival time of the Japanese OBS, and then both time series are transformed into the frequency domain. Spectral division is performed to obtain a correction to apply to other Japanese stations. To avoid peculiarities in the correction from a particular event or

station, we average the spectral division result from five different instruments and events in order to obtain the final correction applied to all of the Japanese data. The correction in amplitude was negligible, and the phase correction is on the order of 1–2 s at short periods ( $\sim 30$ – $45$  s) and increases to  $\sim 3$  s at longer periods ( $\sim 75$ – $90$  s). Careful comparisons of the Japanese data with those of nearby U.S. OBS stations were made after applying the correction to ensure the use of only high-quality data.

[9] After the instrument response was removed, we windowed each seismogram around the Rayleigh wave arrival and then applied a series of 10 mHz narrow band-pass filters centered around select frequencies of interest. We visually inspected each trace and discarded stations with poor signal-to-noise ratio or instrumentation problems at individual events or frequencies. Because the inversion for each frequency is performed separately, it is often possible that for a given event a particular station is used for several adjacent, but not all, frequencies. This individual trace analysis allows us to include many events at longer periods which only recorded the Rayleigh wave above the noise at a few stations.

### 3. Phase Velocity Inversion Methods

[10] We invert for Rayleigh wave phase velocities using the two plane wave method of *Forsyth and Li* [2005]. This technique uses phase and amplitude data from each seismogram to approximate the incoming wavefield as the interference of two best fitting plane waves. Our initial attempts to use a more traditional surface wave analysis which corrects for deviations from the great circle path but assumes a single, planar wavefront [e.g., *Lawrence et al.*, 2006] yielded results which were often inconsistent and unreasonable. Phase velocities were often too high or too low to be believable, and those determined from nearly identical paths sometimes varied greatly. The two plane wave approximation accounts for deviations from the great circle path as well as nonplane wave energy such as multipathing and scattering better than traditional methods [*Li and Detrick*, 2003] and produced better results for our data set. Inversion tests show that residuals in phase are reduced by 30% with the two plane wave method compared to a single plane wave approximation [*Li et al.*, 2003]. The inversion solves for the phase, amplitude, and propagation direction for both of the two plane waves representing each event, as well as the phase velocity averaged over the study area (1-D) and at each inversion node (2-D), and parameters for azimuthal anisotropy. The interference of the plane waves and the resulting vertical displacement is represented as

$$U_z(\omega) = A_1(\omega) \exp[-i(\mathbf{k}_1 \cdot \mathbf{x} - \omega t)] + A_2(\omega) \exp[-i(\mathbf{k}_2 \cdot \mathbf{x} - \omega t)], \quad (1)$$

where  $\mathbf{k}_j$  is the horizontal wavenumber of each wave and  $\mathbf{x}$  is the position vector [*Forsyth and Li*, 2005]. We find that the larger of the two waves most often has a propagation direction less than  $10^\circ$  from the great circle path and there is often some consistency in the direction from period to period for a particular event. The smaller of the two plane waves typically exhibits greater variability; however, often when there is a large difference between the great circle path and

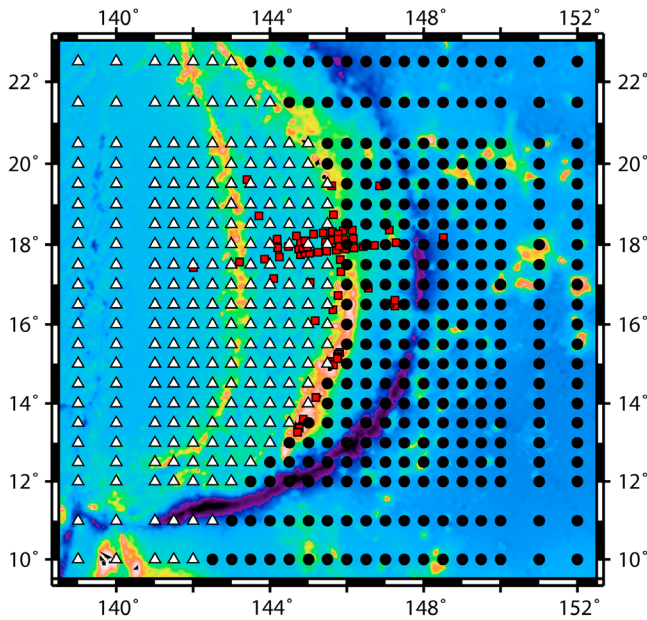


**Figure 4.** Location of nodes used in phase velocity inversion. Black circles denote nodes in the fore-arc subgroup, and white triangles denote nodes in the back-arc subgroup. Dark gray (red) squares mark locations of the stations.

the second plane wave’s propagation direction, the amplitude of this second wave is quite small. This is similar to the results found by Forsyth and Li [2005], who found 95% of primary waves to be within 5° of the great circle path at 28 s and greater variation for the secondary wave. In cases where the two plane wave approximation does not provide a good description of the incoming wavefield, the event for that period is downweighted in the inversion.

[11] Attenuation is accounted for in this study by using a constant surface wave attenuation parameter given by Mitchell [1995]. Further investigation of the surface wave attenuation in the region is given by Pyle [2009]. Inversions allowing laterally varying phase velocities incorporate the use of 2-D finite frequency sensitivity kernels [Yang and Forsyth, 2006b] based on the Born approximation of Zhou et al. [2004]. The use of finite frequency kernels is important for the consideration of Rayleigh wave sensitivity to structure outside of the great circle raypath. The 2-D kernel we use only considers forward scattering of the wavefield, not backscattering; however, the use of the two plane wave method in conjunction with the sensitivity kernels has yielded successful results and reduced residuals in velocity in several previous regional studies [Weeraratne et al., 2007; Yang and Forsyth, 2006a, 2006b].

[12] All inversions are performed using a grid of 506 nodes (Figure 4). The main square of nodes has 0.5° spacing in both latitude and longitude, while the outer edges of the grid have 1° spacing. The more sparsely spaced edges are used to absorb variations in the wavefield which are not well

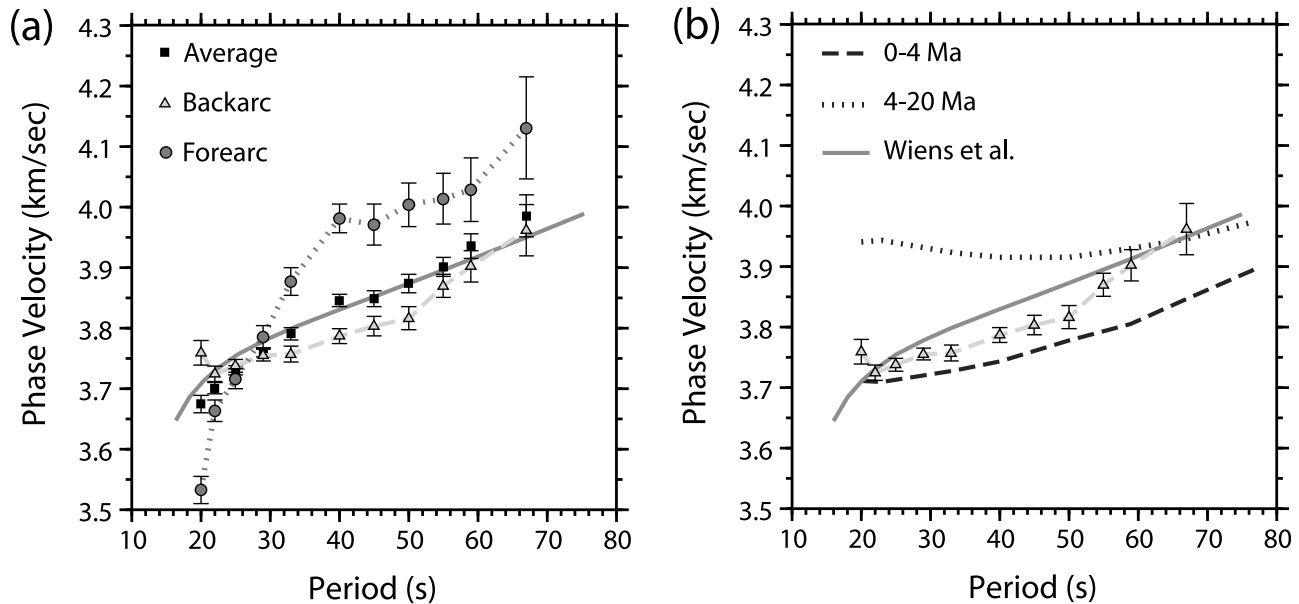


**Figure 5.** (a) Uniform and regional phase velocities as a function of period for the Mariana region. Black squares are the average results from this study. The light gray solid line represents phase velocities predicted by the shear velocity model of Wiens et al. [2006] for the Mariana back arc. Dark gray circles and dotted line are results from the fore-arc region, and light gray triangles and dashed line are from the back-arc region. For all curves, error bars indicate two standard deviations. (b) Back-arc regional phase velocity curve from Figure 5a shown by light gray triangles and dashed line. Phase velocities for 0–4 Ma (black dashed line) and 4–20 Ma (gray dotted line) oceanic crust are from the work of Nishimura and Forsyth [1989]. The solid gray line is the back-arc model predicted from the work of Wiens et al. [2006].

**Table 2.** Average and Regional Phase Velocities

Period (s)	Average $C$ (km/s)	Error (km/s)	Back-Arc $C$ (km/s)	Error (km/s)	Fore-Arc $C$ (km/s)	Error (km/s)
20	3.67	0.015	3.76	0.021	3.53	0.022
22	3.70	0.009	3.72	0.013	3.66	0.018
25	3.73	0.008	3.74	0.010	3.72	0.017
29	3.76	0.008	3.75	0.010	3.79	0.019
33	3.79	0.010	3.76	0.013	3.88	0.023
40	3.84	0.010	3.79	0.013	3.98	0.023
45	3.85	0.013	3.80	0.016	3.97	0.034
50	3.87	0.016	3.82	0.019	4.00	0.036
55	3.90	0.016	3.87	0.019	4.01	0.042
59	3.94	0.021	3.90	0.026	4.03	0.052
67	3.99	0.035	3.96	0.042	4.13	0.084

represented by the two plane wave approximation. The inversion solves for the phase velocity continuously over the study region and is described at each node by interpolating the velocity at any point using a 2-D Gaussian average of neighboring grid points. The scale length used for the averaging function has a trade-off between variance and resolution. After testing a range of scale lengths, we chose a value of 80 km which represents the best compromise between increasing resolution and decreasing variance. The same scale length is also used as a smoothing length in the finite frequency kernels. We also assign an a priori error of 0.2 km/s as moderate damping of the velocity parameters. The inversion for each frequency is performed separately.

[13] The initial inversion solves for an amplitude correction at each station to account for any discrepancies in the assumed instrument responses as well as site effects. Only about 50% of the stations required any amplitude correction, and of those, almost all require only a small amplitude correction that is constant with frequency. Five of the 49 stations required a frequency-dependent correction. Three of these stations were Lamont OBSs: two in the fore arc near Celestial Seamount (Figure 1) and one in the back arc. The other two stations requiring a frequency-dependent correction were land stations located on Rota and Tinian.

## 4. Results

### 4.1. Average Phase Velocities

[14] We begin by inverting for the average Rayleigh wave phase velocity dispersion curve for the entire region. This inversion takes all raypaths for a particular period (Figure 3) and solves for one average velocity for the entire study area, producing the 1-D phase velocity curve as a function of period shown in Figure 5 and listed in Table 2. We used a simple starting model that assumes a phase velocity of 3.8 km/s from 20 to 29 s, 3.9 km/s from 33 to 50 s, and 4.0 km/s from 55 to 67 s. The 1-D inversion is well constrained, and the use of different starting models does not produce significant changes in the outcome. The resulting dispersion curve (Figure 5a) shows that phase velocities

increase steadily from 3.67 km/s at 20 s to 3.98 km/s at 67 s. The 95% confidence interval is smallest (less than 0.3%) at 25–29 s, where simple waveforms and low noise levels allow for the greatest raypath coverage. The errors increase slightly at the shortest period and the longer periods where there is a lower density of observations (Figure 3), but remain less than 1%. Our results are consistent with the phase velocities predicted by the shear velocity model of *Wiens et al.* [2006] determined for the Mariana back arc from regional waveform inversion of the entire wave train, including surface waves (Figure 5a).

[15] We also invert for regional velocities by grouping the grid nodes into two subregions (the back arc and fore arc) based on the structure of the subduction zone (Figure 4). The fore-arc subregion includes the trench and everything east of the active island arc, while the back-arc subregion includes the active volcanic arc, the back-arc spreading center, and everything west of the West Mariana Ridge. We use the uniform dispersion curve result from Figure 5a as a starting model and invert simultaneously for average phase velocities in each subregion. The back-arc dispersion curve is fairly flat between 20 and 33 s, likely due to the thin crust surrounding the back-arc spreading center. Above 30 s, phase velocities increase slowly from 3.75 km/s at 33 s to 3.96 km/s at 67 s. Phase velocities from 25 to 60 s are slightly lower than the those from the model of *Wiens et al.* [2006], reaching a maximum difference of  $\sim 1.5\%$ , but are slightly faster than those predicted by the model of *Nishimura and Forsyth* [1989] for oceanic mantle of age 0–4 Ma (Figure 5b). Above 50 s our back-arc results increasingly approach the phase velocity values of *Nishimura and Forsyth* [1989] for 4–20 Ma. The fore-arc phase velocities increase rapidly from 3.53 km/s at 20 s to  $\sim 4.13$  km/s at 40 s. The curve flattens within error between 40 and 60 s at a value of  $\sim 4$  km/s. Comparison of the two regions shows that the fore arc is characterized by significantly lower phase velocities below 25 s and phase velocities at 30–67 s that are up to 5% higher relative to the arc/back-arc regions. Formal uncertainties for the back-arc subregion curve are comparable to those for the whole

**Figure 6.** Phase velocity maps for 22, 29, 40, and 59 s periods. Maps in the left column show phase velocities, and maps in the right column show standard errors. Velocities are contoured at 0.02 km/s, while errors are contoured at 0.01 km/s. Black squares and triangles mark station locations. The hatched black lines mark the location of the trench, and solid black lines mark the location of the back-arc spreading center. Bathymetry is plotted in gray scale behind velocity and error values. The top color scale is for the velocity plots on the left, and the bottom color scale is for the error plots on the right.

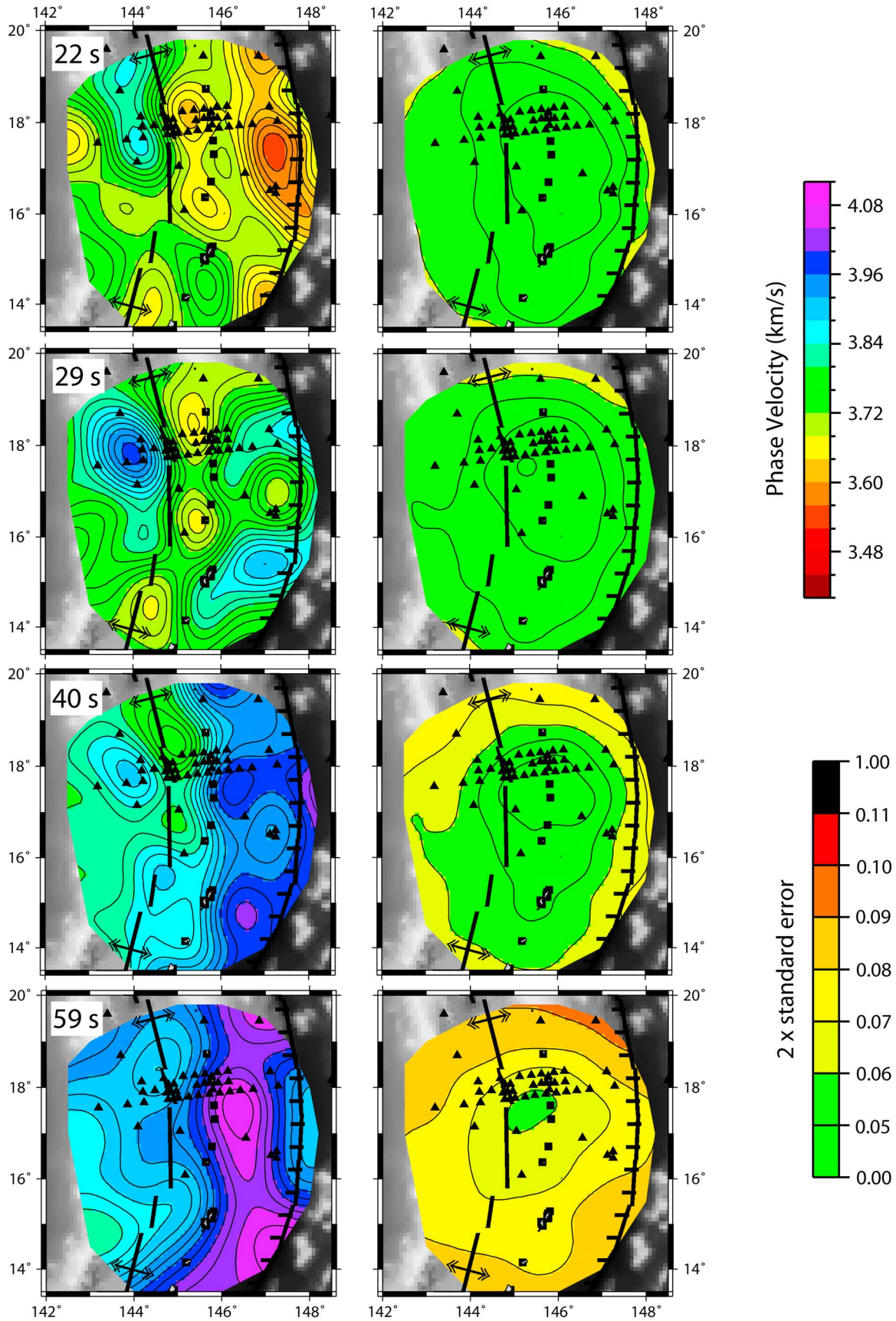
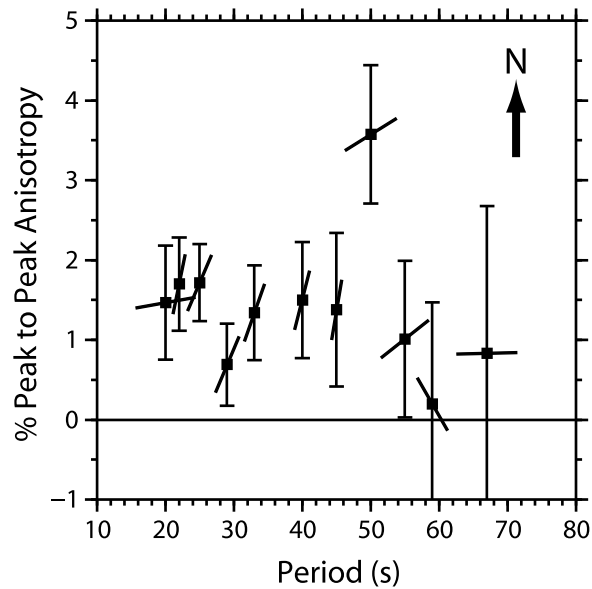


Figure 6



**Figure 7.** Average anisotropy as a function of period. Short bars through each symbol indicate the direction of the fast axis of anisotropy in map view (the arrow indicates the direction of north in map view). Error bars indicate two standard deviations.

region uniform curve, while the fore-arc subregion has slightly higher uncertainties, though they remain below 0.05 km/s for almost all periods.

#### 4.2. Laterally Varying Phase Velocities

[16] The average dispersion curves for the two subregions are used as starting velocities for their respective nodes in an inversion which solves for lateral variations in phase velocity by allowing the velocity to vary at every node. This inversion also incorporates finite frequency sensitivity kernels and includes terms for uniform azimuthal anisotropy. Maps of the phase velocities at each period (Figure 6) are generated by applying a 2-D Gaussian averaging function to interpolate velocities from the inversion nodes to a finer grid. The velocities are masked to show only areas with the best resolution. Estimates of the a posteriori standard error generated from the model covariance matrix and the averaging function are also mapped. The standard error maps (right column of Figure 6) can be used as a tool to help evaluate the resolution of the phase velocity maps (left column) as a function of position. We run a similar inversion using the uniform phase velocities for the entire study area as the starting velocity at every node to test the robustness of our starting model. The major features of the maps (described below) are not strongly dependent on either of these starting models. We choose the regional starting model as our preferred model because it produces lower misfits in the final results than the uniform starting model at most frequencies.

[17] From 20 to 22 s, low velocities throughout the fore arc dominate the phase velocity maps. The transition to faster velocities occurs west of the active island arc. A strong low phase velocity anomaly in the fore arc persists until 29 s near the line of serpentinite seamounts, primarily centered between Celestial and Big Blue. Above 30 s the

velocity contrast east and west of the island arc reverses, with higher velocities in the fore arc at longer periods likely due to sensitivity at increasing depth to high velocities in the subducting slab. Three low-velocity anomalies between the back-arc spreading center and the island arc are prominent at periods of 22–29 s. The northern anomaly occurs near 18.0°N–18.5°N, and the central anomaly is located between roughly 16.0°N and 16.5°N. Velocities in these anomalies reach minimums of about 3.63 km/s at 22 s, and low velocities persist for periods as long as 50 s, but migrate toward the back-arc spreading center. The southern anomaly appears at the edge of our resolution at about 14°N–14.5°N. This anomaly reaches a low velocity of 3.66 km/s at 22–29 s, but it does not extend to periods longer than 30 s within our resolution. Standard errors are smallest in the center of the study area around the dense array of stations which surround Pagan and the back-arc spreading center. The errors increase with increasing period beyond 29 s, partly due to decreased raypath coverage at longer periods, and partly because at longer periods the Fresnel zone is broader, which may smooth out sensitivity to local structure.

#### 4.3. Anisotropy

[18] The inversion for laterally heterogeneous phase velocities includes terms for uniform azimuthal anisotropy averaged over the entire study area (Figure 7). We observe peak-to-peak anisotropy of 0.7%–1.7% for periods of 20–45 s. At these periods the magnitude of anisotropy has a constant average value of about 1.4%. Large anisotropy of 3.5% is found at the 50 s period, but beyond 55 s anisotropy is not resolved from zero at the 95% confidence level. The anomalously high value found at 50 s and the lack of resolution at longer periods is likely due to decreased data density. The fast azimuth is approximately constant at NNE for all periods below 50 s, which is roughly consistent with a trench-parallel direction.

[19] We ran an additional inversion which allowed anisotropy to vary independently in the back-arc and fore-arc regions defined in Figure 4. The results from this inversion are shown in Figure 8. The percentage of anisotropy as a function of period is scattered and is not as well constrained as the uniform average, but we do observe some consistencies in the direction of fast azimuths. From 22 to 45 s we find fast directions in the fore arc that are NNE and trench parallel. At the 50 s period and longer (indicating deeper sensitivity) the fast directions in this region rotate to a trench-perpendicular ENE direction, similar to the average results. One possible explanation is that the longer period results sample deeper in the fore arc and likely show the direction of anisotropy in the subducting slab. Fast directions in the back arc demonstrate the poorest resolution, but they may exhibit a fairly consistent east-west azimuth at periods below 50 s. The magnitude of anisotropy generally increases when the study is divided into regions; however, the directions in the back arc (Figure 8a) are generally close to perpendicular to the directions in the fore arc (Figure 8b), resulting in the smaller average as observed in Figure 7. Although results for regionalized anisotropy are poorly constrained compared to the uniform anisotropy results, tests show that observations which are consistent in azimuth between three to four periods may indicate structure that is real [Weeraratne et al., 2003].

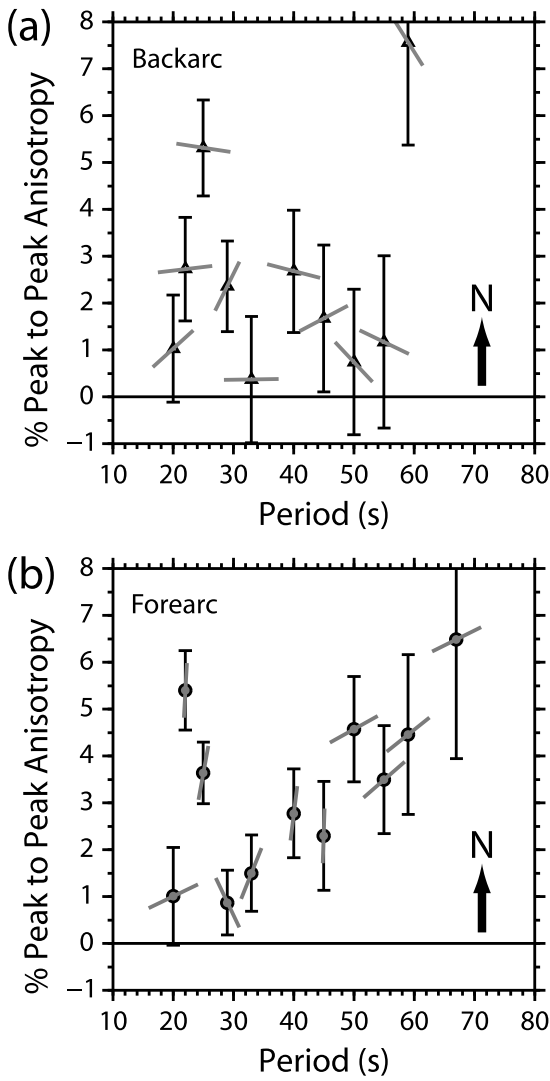


**Figure 8.** Anisotropy as a function of period for the (a) back-arc and (b) fore-arc regions. Short bars through each symbol indicate the direction of the fast axis of anisotropy in map view (the arrow indicates the direction of north in map view). Error bars indicate two standard deviations. The 67 s point in the back arc is outside the displayed scale.

**4.4. One-Dimensional Average Shear Velocity Models**

[20] We invert the uniform and regional phase velocity curves for shear velocity using the work of *Saito* [1988] and the method of *Weeraratne et al.* [2003]. The inversion is an iterative process that first predicts phase velocities based on

**Figure 9.** (a) Average shear velocity as a function of depth. The gray dashed line shows the starting model from the work of *Wiens et al.* [2006]. Boxes indicate two standard deviations from the average velocities over well-resolved depth ranges. (b) Examples of resolution kernels at 32 and 90 km. (c) Shear velocity curves for the back-arc and fore-arc regions. The solid black line indicates our average shear velocity model from Figure 9a, light gray triangles represent the back-arc model, and dark gray circles represent the fore-arc model.

a starting shear velocity model and then uses a damped least squares inversion to find changes to the shear velocity model which produce the best fit between the predicted and

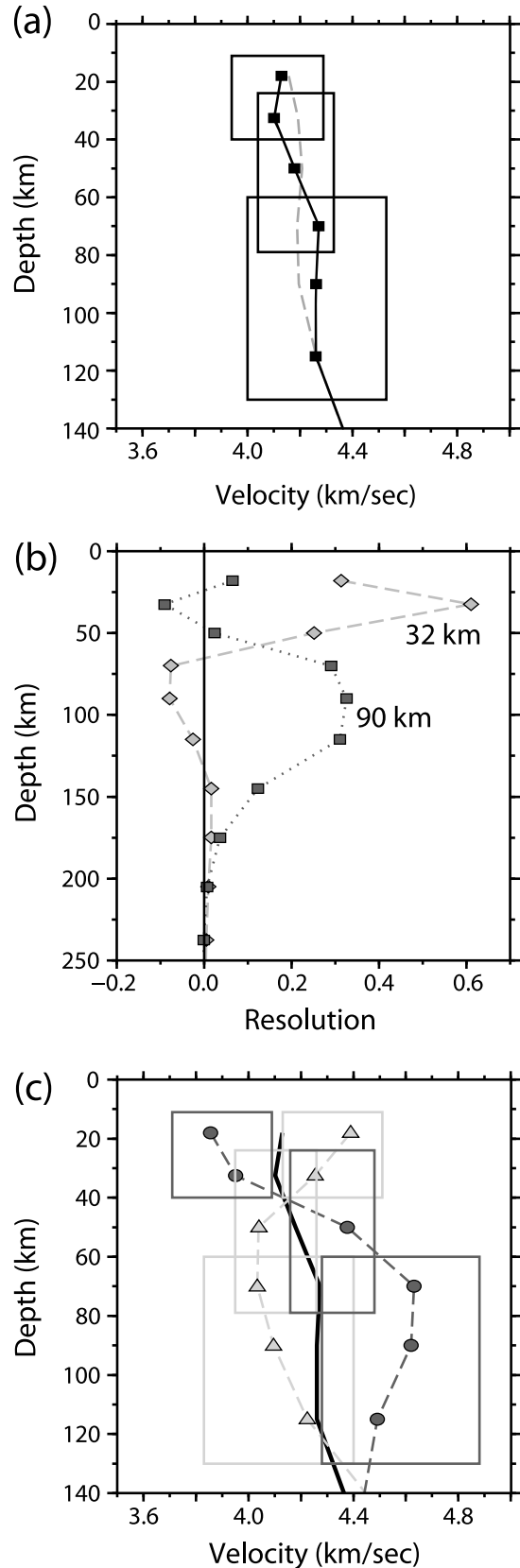


**Table 3.** Average and Regional Shear Wave Velocities

Depth (km)	Average $V_s$ (km/s)	Error (km/s)	Back-Arc $V_s$ (km/s)	Error (km/s)	Fore-Arc $V_s$ (km/s)	Error (km/s)	Depth Range (km)
18.0	4.13	0.088	4.39	0.095	3.86	0.097	12–27
32.5	4.10	0.096	4.25	0.099	3.95	0.102	24–42
50.0	4.18	0.098	4.04	0.106	4.38	0.110	38–67
70.0	4.27	0.131	4.03	0.143	4.63	0.147	50–85
90.0	4.26	0.161	4.10	0.169	4.62	0.172	79–128
115.0	4.26	0.167	4.49	0.175	4.49	0.178	96–146

measured phase velocities (from sections 4.1 and 4.2). We use the shear velocity model determined for the Mariana back arc from waveform inversion [Wiens *et al.*, 2006] (Figure 9a, dashed line) as a starting model. The model has  $P$  wave velocities that are consistent with results from active source studies [Calvert *et al.*, 2008; Takahashi *et al.*, 2007] and includes a 3 km water layer and two crustal layers with thicknesses of 4 and 3 km and fixed shear velocities of 2.9 and 3.7 km/s, respectively. Since Rayleigh wave phase velocities are primarily sensitive to shear velocity, we assume that the  $P$  velocities in the mantle are  $\sqrt{3}$  multiplied by the shear velocity. Rayleigh wave velocities are also only weakly sensitive to density compared to other factors; therefore, we assume a density model which does not vary from iteration to iteration. We investigate a range of damping parameters in the form of a priori uncertainties for the initial values of the velocity parameters and select 0.2 km/s as the best compromise between decreasing variance and increasing resolution. Each iteration is damped to the starting model. The inversion also incorporates second-derivative smoothing with nonzero off-diagonals that are one third of the values of the diagonal terms in the model covariance matrix, providing some correlation between changes in adjacent depth layers.

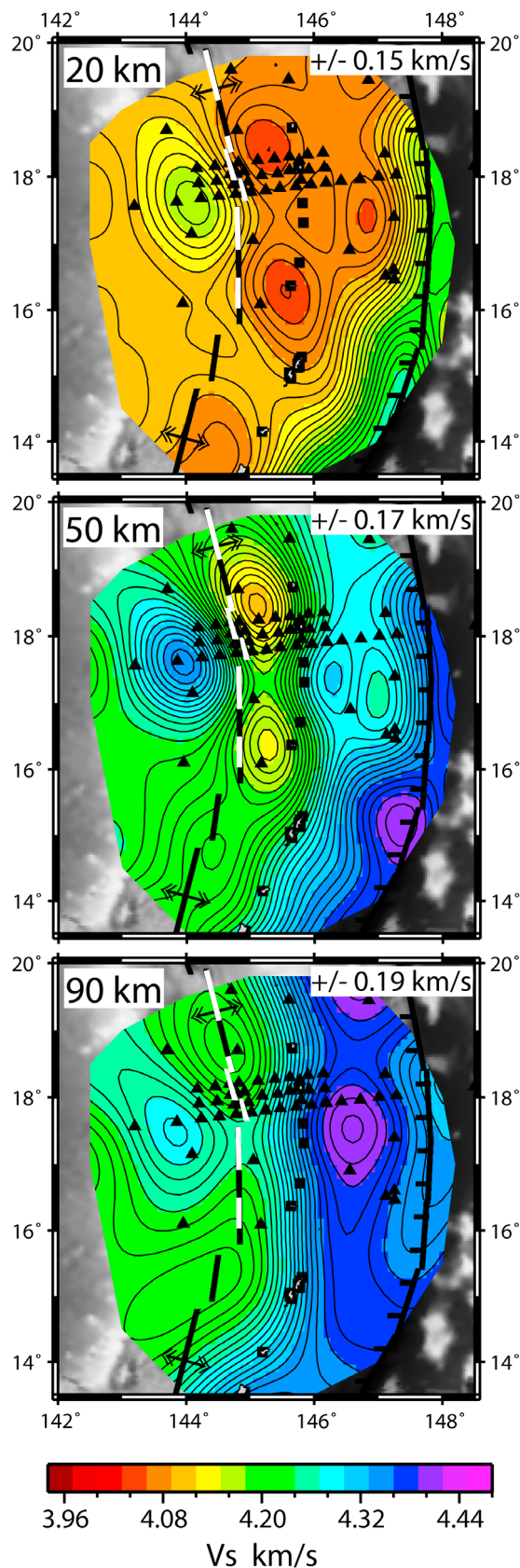
[21] The first shear wave inversion determines an average velocity structure across the entire study area using the measured phase velocities from Figure 5a. Shear velocities of  $4.1 \pm 0.1$  km/s are observed from 20 to 40 km depth, gradually increasing to  $4.35 \pm 0.1$  km/s at 70 km (Figure 9a). Very little change from the starting model is observed. Shear wave velocities averaged over the study area do not exhibit strong changes in velocity with depth, likely due to the averaging of highly variable structure in the region. To test this, we use the average 1-D shear velocity model as the starting model to invert the regional phase velocity curves in the fore arc and back arc (Figure 5a, circles and triangles) for shear velocity structure (Figure 9c). The fore arc (Figure 9c, circles) has velocities which reach as low as  $3.86 \pm 0.1$  km/s at a depth of 18 km with a well-resolved sharp increase to values of nearly  $4.65 \pm 0.1$  km/s at 70 km depth. The velocities then suggest a 2% negative velocity gradient below 90 km depth which approaches the starting model but is poorly resolved within 95% confidence. The back arc (Figure 9c, triangles) shows a negative velocity gradient from  $4.38 \pm 0.1$  km/s at 20 km depth to a low velocity zone of  $4.03 \pm 0.1$  km/s between 50 and 70 km. Below 90 km, velocities increase with increasing depth, approaching the starting model at a depth of 115 km. These 1-D inversions for shear velocity constrain only average  $S_v$  structure and do not take into account the effects of anisotropy. However, because anisotropy as a function of period appears to be roughly constant at 1.4% within error (Figure 7),

we expect that the shape of the velocity curves with depth will remain unchanged. This confidence includes variation of anisotropy values within the error bars depicted.

[22] Confidence in shear wave velocities is shown by boxes which represent  $\pm 2$  standard deviations from the average velocities over well-resolved depth ranges. Uncertainties in depth are given by the width of resolution kernels. Examples of these kernels for velocities at 32 and 90 km are plotted in Figure 9b. Rayleigh waves have peak sensitivity to a depth which is approximately 4/3 of the period, but they remain sensitive to a finite range of depths surrounding the peak depth. At shallow depths this range is narrow, as shown by the resolution kernel for 32 km depth in Figure 9b. As depth increases, the width of the kernels increases and sensitivity to a particular depth decreases. Average and regional shear wave velocities, and the depth range of resolution for each point, are listed in Table 3.

#### 4.5. Laterally Varying Shear Velocities

[23] Shear velocity maps are constructed using 1-D inversions of phase velocities at each of the inversion nodes (Figure 10). As a starting model for these inversions, we use the average shear velocity model for the region (Figure 9a). The three upper layers representing the water and two crustal layers have fixed velocities with thicknesses modified at each node for varying water depths and crustal thicknesses based on the model given by Takahashi *et al.* [2007]. Small differences in the thicknesses of these layers make very little difference in the resulting shear velocity curves, except at the trench where the depth of the water layer more than doubles. The variation in depth resolution kernels (Figure 9b) results in each map representing an average over a range of depths as indicated in Table 3. The fore arc exhibits a low velocity anomaly near the trench that decreases in magnitude for depths greater than 30 km. Below 40 km the fore arc is mainly characterized by high velocities associated with the subducting slab which are shallowest near the trench and move gradually westward with increasing depth. Two low shear velocity anomalies are observed between the back-arc spreading center and island arc located at about 18.0°N–18.5°N latitude extending to a depth of 115 km and at about 16.0°N–16.5°N extending to about 70 km depth. A third low velocity anomaly can also be seen at about 14.0°N–14.5°N between the spreading center and the island arc. This anomaly is weaker and more diffuse than the other two anomalies and reaches the limits of our resolution, but it may extend to at least 50 km depth. Below 70 km the southernmost anomaly and the central anomaly may merge, although this is likely due to decreasing lateral resolution as depth increases. All three low velocity anomalies appear to move westward toward the spreading



center as depth increases. A high velocity anomaly is also observed at about 17.5°N near the West Mariana Ridge.

[24] We put together a shear velocity cross section in the same manner as the maps using the point by point 1-D inversions of phase velocities at each of the inversion nodes along the 18°N latitude line (Figure 11). The eastern portion of the cross section is dominated by high velocities deeper than 30 km which reach almost 4.5 km/s in the subducting slab. The fore arc has a low velocity anomaly with velocities that reach as low as 4.05 km/s at shallow depths extending to around 35–40 km just above the slab. Beneath the back-arc spreading center and volcanic arc the cross section shows a pronounced low velocity zone exhibiting velocities as low as 4.0 km/s, with the lowest velocities between depths of about 20 and 70 km. The peak of this low velocity anomaly in the maps and cross section (~30 km) appears to be slightly shallower than for the 1-D inversion (~50–70 km), but we believe that this is due to higher uncertainties and vertical smoothing when inverting for 2-D shear velocities. Phase velocity curves from individual nodes (Figure 6) have higher uncertainty compared to phase velocity curves which average over a group of nodes (Figure 5). Owing to this increased uncertainty, the inversion of individual nodes for shear velocities is more dependent on the smoother average starting model, and thus the resulting velocities have poorer vertical resolution. The decrease in resolution reduces the appearance of the high velocity lid in the shear velocity maps and cross section.

## 5. Discussion

### 5.1. Back Arc and Arc

[25] The phase velocities and structure found by this study in the back-arc region are relatively similar to the results of *Isse et al.* [2004], which relied on only the station at Guam (GUMO) and one OBS for the Mariana portion of the study. They found phase velocities over the spreading center ranging from 3.6 km/s at 25 s to 3.75 km/s at 50 s, in comparison to phase velocities ranging from 3.64 to 3.76 km/s along the back-arc spreading center from our maps of lateral variation (Figure 6). Based on a larger surface wave data set and an inversion for 3-D velocity structure, *Isse et al.* [2009] found shear velocities of ~4.1 km/s between 80 and 120 km depth. The magnitude agrees with our observed shear velocities, but the depth of the anomaly extends much deeper than the anomaly we observe. However, their study has lower resolution in the Mariana region due to the large area of study and the use of source-to-receiver paths. Shear velocity tomography using local and teleseismic body waves recorded

**Figure 10.** Shear wave velocity maps. The depth range of resolution for each map is indicated in Table 3. Velocities are contoured at 0.01 km/s. Black triangles and squares mark locations of stations. The hatched black lines mark the location of the trench, and the solid black and white lines mark the location of the back-arc spreading center. White portions along the spreading center indicate sections along the axis where *Kitada et al.* [2006] finds gravity bull's-eye-like behavior. Gray-scale bathymetry is plotted behind velocities.

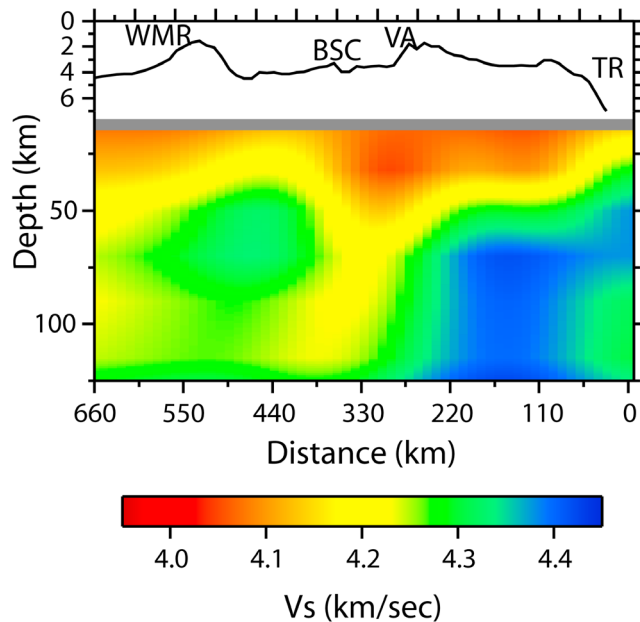


**Figure 11.** Shear wave velocity cross section along the 18°N latitude line. Exaggerated bathymetry is shown along the top for reference. Main tectonic features are labeled as West Mariana Ridge (WMR), back-arc spreading center (BSC), volcanic arc (VA), and trench (TR).

by the Mariana experiment shows low velocities primarily beneath the volcanic arc of about 4.0–4.2 km/s between depths of 25 and 80 km [Barklage *et al.*, 2006]. This body wave tomographic study supports both the depth and magnitude of low shear velocities we find from surface wave analysis.

[26] The surface wave phase velocities determined here can be compared to phase velocities along mid-ocean ridges to evaluate any systematic differences in upper mantle structure. Nishimura and Forsyth [1989] find phase velocities of 3.71–3.77 km/s at 20–50 s using land stations which recorded paths passing along the East Pacific Rise at ages of 0–4 Ma. A better comparison is afforded by recent results from a joint inversion of data from the Mantle Electromagnetic and Tomography Experiment (MELT) and Gravity Lineations, Intraplate Melting, Petrology and Seismology Expedition (GLIMPSE) OBS experiments along the East Pacific Rise [Harmon *et al.*, 2009] which uses the same array analysis method and has similar spatial resolution to those shown in this paper. The study by Harmon *et al.* [2009] shows phase velocities from just over 3.6 km/s at 22 s to about 3.8 km/s at 50 s along the ridge axes. These are the same velocities we find at the lowest velocity region along the Mariana trough (Figure 12), suggesting little difference between the seismic structure of the Mariana trough axis and the East Pacific Rise axis. When inverted for shear structure, our results show a low velocity region extending from 20 to 70 km depth (Figure 10) and reaching a minimum velocity at about 32 km, which agrees well with the depth range of primary melt production expected at mid-ocean ridges from the geochemical results of Shen and Forsyth [1995]. These depths are also similar to the depths of low shear velocities

found beneath the East Pacific Rise [Conder *et al.*, 2002; Gu *et al.*, 2005; Hammond and Toomey, 2003].

[27] The primary features observed in the arc and back-arc region are low velocity anomalies located between the back-arc spreading center and the island arc. The anomalies appear at approximately 18.0°N–18.5°N, 16.0°N–16.5°N, and 14.0°N–14.5°N latitude. The southernmost anomaly is near the edge of our resolution; however, we have sufficient crossing raypath coverage (Figure 3) to resolve this anomaly at the 95% confidence level at periods below 30 s.

[28] The locations in latitude of all three anomalies correspond to the locations of low values of mantle Bouguer anomalies along the back-arc spreading center reported by Kitada *et al.* [2006]. Two of the locations are similar to gravity anomalies that have been reported previously in studies along the Mid-Atlantic Ridge [Kuo and Forsyth, 1988; Lin *et al.*, 1990]. The anomalies take the shape of a “bull’s-eye” pattern centered along an active linear ridge segment, and they are thought to represent concentrated upwellings of magma. This proposed type of upwelling also explains variations in crustal thickness that are observed with a thicker crust occurring near the center of the upwelling and a progressive along-axis crustal thinning away from the center of the spreading segment [e.g., Kuo and Forsyth, 1988; Lin *et al.*, 1990; Tolstoy *et al.*, 1993]. Kitada *et al.* [2006] used gravity data to examine crustal thickness variations and compared mantle Bouguer anomalies and spreading segment lengths in the Marianas with other studies which also noted the bull’s-eye anomalies [Detrick *et al.*, 1995; Lin *et al.*, 1990] and found that several segments fit the trends in gravity anomalies while others appear to be magma-starved. Among those segments with bull’s-eye-feature-like trends are those extending from 18.0°N–18.5°N and 16.0°N–16.3°N. In addition, geochem-

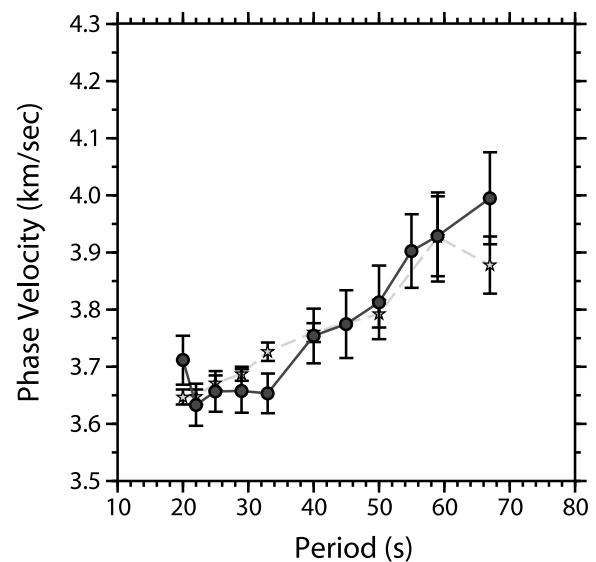


**Figure 12.** Comparison of phase velocities between the Marianas and the East Pacific Rise. Black circles represent values taken from the northernmost velocity anomaly in the Mariana back arc. Gray stars represent values closest to the ridge axis of the East Pacific Rise from Harmon *et al.* [2009].

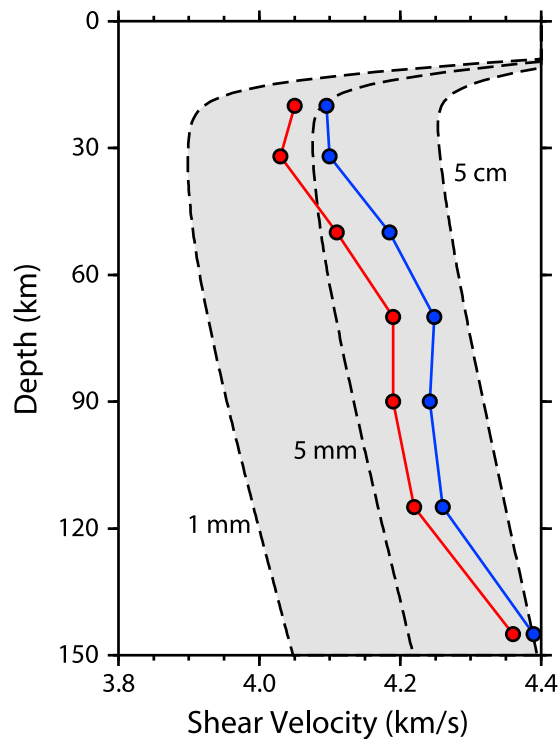


**Figure 13.** Comparison of measured shear velocities with velocities predicted by the model of *Faul and Jackson* [2005]. The shaded gray area represents the range of velocities predicted for 1 Myr old oceanic crust with grain sizes ranging from 1 mm to 5 cm. Black dashed lines represent specific velocity curves at 1 mm, 5 mm, and 5 cm. The dark gray (red) circles represent shear velocities taken from the northernmost ( $\sim 18.0^{\circ}\text{N}$ – $18.5^{\circ}\text{N}$ ) low velocity anomaly in the back arc. The white (blue) circles represent shear velocities taken from a point along the spreading center in between the major low velocity anomalies ( $\sim 17^{\circ}\text{N}$ ).

ical surveys have reported areas of increased melting between  $16^{\circ}\text{N}$  and  $17^{\circ}\text{N}$  [*Gribble et al.*, 1996] and near  $18^{\circ}\text{N}$  [*Stolper and Newman*, 1994]. These areas fall at the same location of two of our phase velocity anomalies which likely indicate the presence of melt. The southernmost low velocity anomaly at  $14.0^{\circ}$ – $14.5^{\circ}\text{N}$  does not correspond to a bull's-eye gravity anomaly, but it does correspond to a region with a relatively low mantle Bouguer anomaly and higher crustal thickness averages which *Kitada et al.* [2006] interpret as an area of higher magmatic activity with a sheet-like upwelling similar to fast spreading ridges. The correlation between low velocity anomalies that we observe to depths of at least 50 km and up to 90 km in some places, low Bouguer gravity anomalies, and geochemical surveys suggests that these are areas of higher melting and that the amount of melting is highly laterally variable along the Mariana trough.

[29] To more closely examine the indication of melt beneath the low velocity anomalies we observe near the spreading center, we compute shear velocities predicted by the model of *Faul and Jackson* [2005] which describes the shear modulus and attenuation with variations in frequency, temperature, and grain size. For our model we calculate a geotherm using a mantle potential temperature of  $1350^{\circ}\text{C}$

determined for the Mariana back arc using major element chemistry of back-arc basin basalts [*Kelley et al.*, 2006]. We vary frequency with depth using the peak depth sensitivities of surface waves. For all other parameters we use physical constants provided by *Faul and Jackson* [2005] and calculate a range of velocities for 1 Myr old oceanic crust using different grain sizes. The model is shown in Figure 13 for grain sizes from 1 mm to 5 cm. Shear velocities determined from our inversions near the back-arc spreading center from the  $18.0^{\circ}\text{N}$ – $18.5^{\circ}\text{N}$  low velocity anomaly as well as the area between the two strong low velocity anomalies around  $17^{\circ}\text{N}$  are plotted for comparison.

[30] The resulting modeled velocities show a strong dependence on grain size, and both of the measured velocity curves fall within the range of velocities expected for grain sizes appropriate for the upper mantle. If the grain size is small enough ( $<4$  mm), no melt is required to fit our observations. However, if the grain size is slightly larger, the shear velocities we observe, particularly from  $\sim 30$  to 50 km depth at the low velocity anomaly, might indicate the presence of melt. Similar shear velocities of  $\sim 4.0$ – $4.1$  km/s are seen to depths of  $\sim 60$  km just beneath the southern East Pacific Rise in a study using Love waves by *Dunn and Forsyth* [2003]. Their study uses a different temperature scaling relationship but also finds that these velocities may suggest a small amount of melting.

[31] The anomalies on the phase and shear velocity maps, as well as the cross section, show no distinction between the back-arc spreading center and the volcanic arc although preliminary body wave tomography results suggest that there are two separate low velocity anomalies [*Barklage et al.*, 2006], and seismic attenuation tomography also shows two separate anomalies [*Pozgay et al.*, 2009]. Our surface wave tomography results do not have the lateral resolution to distinguish between possible regions of separate back-arc melting and volcanic arc melting over this small area. The wavelength for Rayleigh waves used in this study ranges from about 30 to 90 km for increasing periods from 20 to 67 s, which is close to the separation distance of these two regions. At greater depths the shear velocity anomalies move gradually closer to the back-arc spreading center, suggesting that between 50 and 70 km the low velocities are probably entirely attributed to the spreading center.

## 5.2. Fore Arc

[32] In the fore arc, the Rayleigh wave phase velocity maps at periods below 30 s show a strong low velocity anomaly near the trench between the Big Blue and Celestial seamounts. These low velocities are seen in the average shear velocity curve for the fore-arc region with values as low as 3.85 km/s and in the cross section and shear velocity maps to depths of around 35–40 km. Such low velocities cannot result from thick crust, since marine seismic studies of the fore arc show a crustal thickness of about 15 km [*Takahashi et al.*, 2007; *Calvert et al.*, 2008]. Preliminary results from body wave tomography also show a region of low velocities in the fore arc beneath Big Blue Seamount [*Barklage et al.*, 2006].

[33] The Mariana system is well-known for its active serpentinite mud volcanoes, such as Big Blue, which are located throughout the fore arc [*Fryer*, 1996; *Fryer et al.*, 1999]. Serpentinite is a hydrated form of peridotite and is

known to exhibit lower seismic velocities than peridotite (for depths we are concerned with in the fore arc, the velocity of serpentinite might be 2.38–2.41 km/s while velocities for peridotite might range from 4.46 to 4.68 km/s [Christensen, 1966]). Many other subduction zones also show decreased shear velocities in the fore arc, thought to be due to serpentinization [Hyndman and Peacock, 2003]. In the Marianas, Fryer *et al.* [1999] suggest that the muds at the seamounts are derived directly from fluids which have a slab source between 15 and 25 km deep near the trench. In addition, a study from *P* to *S* converted waves also finds shear wave velocities as low as 3.6 km/s to depths of 50 km above the slab near the islands of Saipan and Tinian [Tibi *et al.*, 2008]. This extends slightly deeper than our observed low velocities, but the anomaly in our results is located closer to the trench where the slab is shallower. Studies of the crustal structure from active source seismic profiling over the volcanic arc [Calvert *et al.*, 2008] and along a profile from the fore arc to west of the West Mariana Ridge [Takahashi *et al.*, 2007] also find lowered upper mantle *P* wave velocities, although their resolution in the fore arc is limited.

### 5.3. Anisotropy

[34] Our average results for the region suggest peak-to-peak anisotropy between 1% and 2%, with an average of 1.4% for periods below 50 s, which agrees well with the magnitude of anisotropy estimated from shear wave splitting results in the region. Pozgay *et al.* [2007] found 1.0%–1.6% anisotropy using data from the same deployment, and earlier studies using the station GUMO on Guam reported 0.6%–2.25% anisotropy [Fouch and Fischer, 1998]. Previous shear wave splitting studies suggest that the azimuthal anisotropy is spatially variable in this region. Pozgay *et al.* [2007] found fast directions to be mostly arc-parallel in the arc and back-arc spreading center regions with arc-perpendicular fast directions appearing in the far back arc to the west of the back-arc spreading center, and Volti *et al.* [2006] found arc-perpendicular fast directions beneath the ridge axis and fast directions aligned with the absolute plate motion of the Pacific plate (NW) farther into the back arc. Fouch and Fischer [1998] and Xie [1992] found fast directions that were roughly parallel to the absolute plate motion in the Guam region. Based on the regionalized anisotropic inversion, it appears that the fast direction for our average results is dominated by anisotropy in the fore arc and that the fore arc may be characterized by a fast anisotropy direction parallel to the arc. Results in the back arc show a fast direction roughly parallel to the absolute plate motion, consistent with the shear wave splitting results of Pozgay *et al.* [2007] and other previous studies in the region.

## 6. Conclusions

[35] We are able to obtain good Rayleigh wave phase and shear wave velocities from data recorded by the combined land- and marine-based Mariana experiment. The phase velocities exhibit good agreement with values determined from the East Pacific Rise. Velocities are lowest between the back-arc spreading center and the volcanic arc at three main locations which coincide with the locations of low Bouguer gravity anomalies, suggesting that the gravity and seismic

velocity anomalies mark areas of higher melt than other regions along the Mariana trough. The shear velocities obtained from inversion of the phase velocities indicate that the region of melt beneath the spreading center and volcanic arc extends to at least 50 km and in the northern region, where our resolution is best, to at least 90 km, with the region of lowest velocities located at 20–70 km depth. Low velocities also appear at uppermost mantle depths in the fore arc and are likely associated with serpentinization of fore-arc mantle, as suggested by the presence of serpentinite seamounts.

[36] **Acknowledgments.** We thank Donald Forsyth and Yingjie Yang for comments and help on implementing the two plane wave method. We would also like to thank the numerous people involved in the deployment and collection of the seismographs. James Gaherty and an anonymous reviewer provided thorough and helpful reviews which greatly improved the quality of the manuscript. This research was conducted with support from the MARGINS program under NSF grant OCE0001938.

## References

- Barklage, M. E., J. A. Conder, D. A. Wiens, P. J. Shore, H. Shiohara, H. Sugioka, and H. Zhang (2006), 3-D seismic tomography of the Mariana mantle wedge from the 2003–2004 passive component of the Mariana subduction factory imaging experiment, *Eos Trans. AGU*, 87(52), Fall Meet. Suppl., Abstract T23C-0506.
- Bloomer, S. H., R. J. Stern, and N. C. Smoot (1989), Physical volcanology of the submarine Mariana and Volcano arcs, *Bull. Volcanol.*, 51, 210–224.
- Calvert, A. J., S. L. Klemperer, N. Takahashi, and B. C. Kerr (2008), Three-dimensional crustal structure of the Mariana island arc from seismic tomography, *J. Geophys. Res.*, 113, B01406, doi:10.1029/2007JB004939.
- Christensen, N. I. (1966), Elasticity of ultrabasic rocks, *J. Geophys. Res.*, 71(24), 5921–5931.
- Conder, J. A., D. W. Forsyth, and E. M. Parmentier (2002), Asthenospheric flow and asymmetry of the East Pacific Rise, MELT area, *J. Geophys. Res.*, 107(B12), 2344, doi:10.1029/2001JB000807.
- Detrick, R. S., H. D. Needham, and V. Renard (1995), Gravity anomalies and crustal thickness variations along the Mid-Atlantic Ridge between 33°N and 40°N, *J. Geophys. Res.*, 100(B3), 3767–3787.
- Dunn, R. A., and D. W. Forsyth (2003), Imaging the transition between the region of mantle melt generation and the crustal magma chamber beneath the southern East Pacific Rise with short-period Love waves, *J. Geophys. Res.*, 108(B7), 2352, doi:10.1029/2002JB002217.
- Engdahl, E. R., R. D. v. d. Hilst, and R. Buland (1998), Global teleseismic earthquake relocation with improved travel times and procedures for depth determination, *Bull. Seismol. Soc. Am.*, 88, 722–743.
- Faul, U. H., and I. Jackson (2005), The seismological signature of temperature and grain size variations in the upper mantle, *Earth Planet. Sci. Lett.*, 234, 119–134.
- Forsyth, D. W., and A. Li (2005), Array analysis of two-dimensional variations in surface wave phase velocity and azimuthal anisotropy in the presence of multipathing interference, in *Seismic Earth Array Analysis of Broadband Seismograms*, edited by A. Levander and G. Nolet, pp. 81–97, AGU, Washington, D. C.
- Fouch, M. J., and K. M. Fischer (1998), Shear wave anisotropy in the Mariana subduction zone, *Geophys. Res. Lett.*, 25(8), 1221–1224.
- Fryer, P. (1996), Evolution of the Mariana convergent plate margin system, *Rev. Geophys.*, 34(1), 89–125.
- Fryer, P., C. G. Wheat, and M. J. Mottl (1999), Mariana blueschist mud volcanism: Implications for conditions within the subduction zone, *Geology*, 27(2), 103–106.
- Gribble, R. F., R. J. Stern, S. H. Bloomer, D. Stuben, T. O’Hearn, and S. Newman (1996), MORB mantle and subduction components interact to generate basalts in the southern Mariana Trough back-arc basin, *Geochim. Cosmochim. Acta*, 60(12), 2153–2166.
- Gu, Y. J., S. C. Webb, A. L. Lerner-Lam, and J. B. Gaherty (2005), Upper mantle structure beneath the eastern Pacific ocean ridges, *J. Geophys. Res.*, 110, B06305, doi:10.1029/2004JB003381.
- Hammond, W. C., and D. R. Toomey (2003), Seismic velocity anisotropy and heterogeneity beneath the Mantle Electromagnetic and Tomography Experiment (MELT) region of the East Pacific Rise from analysis of *P* and *S* body waves, *J. Geophys. Res.*, 108(B4), 2176, doi:10.1029/2002JB001789.

- Harmon, N., D. W. Forsyth, and D. S. Weeraratne (2009), Thickening of young Pacific lithosphere from high-resolution Rayleigh wave tomography: A test of the conductive cooling model, *Earth Planet. Sci. Lett.*, *278*, 96–109.
- Husen, S., R. Quintero, E. Kissling, and B. R. Hacker (2003), Subduction zone structure and magmatic processes beneath Costa Rica constrained by local earthquake tomography and petrological modeling, *Geophys. J. Int.*, *155*, 11–32.
- Hyndman, R. D., and S. M. Peacock (2003), Serpentinization of the forearc mantle, *Earth Planet. Sci. Lett.*, *212*, 417–432.
- Isse, T., H. Shiobara, Y. Fukao, K. Mochizuki, T. Kanazawa, H. Sugioka, S. Kodaira, R. Hino, and D. Suetsugu (2004), Rayleigh wave phase velocity measurements across the Philippine sea from a broad-band OBS array, *Geophys. J. Int.*, *158*, 257–266.
- Isse, T., et al. (2009), Seismic structure of the upper mantle beneath the Philippine Sea from seafloor and land observation: Implications for mantle convection and magma genesis in the Izu-Bonin-Mariana subduction zone, *Earth Planet. Sci. Lett.*, *278*, 107–119.
- Iwamoto, H., M. Yamamoto, N. Seama, K. Kitada, T. Matsuno, Y. Nogi, T. Goto, T. Fujiwara, K. Suyehiro, and T. Yamazaki (2002), Tectonic evolution of the central Mariana Trough, *Eos Trans. AGU*, *83*(47), Fall Meet. Suppl., Abstract T72A-1235.
- Kelley, K. A., T. Plank, T. L. Grove, E. Stolper, S. Newman, and E. Hauri (2006), Mantle melting as a function of water content beneath back-arc basins, *J. Geophys. Res.*, *111*, B09208, doi:10.1029/2005JB003732.
- Kitada, K., N. Seama, T. Yamazaki, Y. Nogi, and K. Suyehiro (2006), Distinct regional differences in crustal thickness along the axis of the Mariana Trough, inferred from gravity anomalies, *Geochem. Geophys. Geosyst.*, *7*, Q04011, doi:10.1029/2005GC001119.
- Kuo, B.-Y., and D. W. Forsyth (1988), Gravity anomalies of the ridge-transform system in the south Atlantic between 31 and 34.5 S: Upwelling centers and variations in crustal thickness, *Mar. Geophys. Res.*, *10*, 205–232.
- Lawrence, J. F., D. A. Wiens, A. A. Nyblade, S. Anandkrishnan, P. J. Shore, and D. Voigt (2006), Rayleigh wave phase velocity analysis of the Ross Sea, Transantarctic Mountains and East Antarctica from a temporary seismograph array, *J. Geophys. Res.*, *111*, B06302, doi:10.1029/2005JB003812.
- Li, A., and R. S. Detrick (2003), Azimuthal anisotropy and phase velocity beneath Iceland: Implication for plume-ridge interaction, *Earth Planet. Sci. Lett.*, *214*, 153–165.
- Li, A., D. W. Forsyth, and K. M. Fischer (2003), Shear velocity structure and azimuthal anisotropy beneath eastern North America from Rayleigh wave inversion, *J. Geophys. Res.*, *108*(B8), 2362, doi:10.1029/2002JB002259.
- Lin, J., G. M. Purdy, H. Schouten, J. C. Sempere, and C. Zervas (1990), Evidence from gravity data for focused magmatic accretion along the Mid-Atlantic Ridge, *Nature*, *344*, 627–632.
- McCaffrey, R. (1996), Estimates of modern arc-parallel strain rates in forearcs, *Geology*, *24*, 27–30.
- Meijer, A. (1982), Mariana-Volcano Islands, in *Andesites*, edited by R. S. Thorpe, pp. 293–306, John Wiley, New York.
- Mitchell, B. J. (1995), Anelastic structure and evolution of the continental crust and upper mantle from seismic surface wave attenuation, *Rev. Geophys.*, *33*(4), 441–462.
- Nishimura, C. E., and D. W. Forsyth (1989), The anisotropic structure of the upper mantle in the Pacific, *Geophys. J.*, *96*, 203–229.
- Pozgay, S. H., D. A. Wiens, J. A. Conder, H. Shiobara, and H. Sugioka (2007), Complex mantle flow in the Mariana subduction system: Evidence from shear wave splitting, *Geophys. J. Int.*, *170*(1), 371–386.
- Pozgay, S. H., D. A. Wiens, J. A. Conder, H. Shiobara, and H. Sugioka (2009), Seismic attenuation tomography of the Mariana subduction system: Implications for thermal structure, volatile distribution, and slow-spreading dynamics, *Geochem. Geophys. Geosyst.*, *10*, Q04X05, doi:10.1029/2008GC002313.
- Pyle, M. L. (2009), *Seismic Surface Wave Studies of the Mariana Mantle Wedge and the Transantarctic Mountains*, 144 pp., Washington Univ. in St. Louis, St. Louis, Mo.
- Reyners, M. (2006), Imaging subduction from the trench to 300 km depth beneath the central North Island, New Zealand with  $V_p$  and  $V_p/V_s$ , *Geophys. J. Int.*, *165*, 565–583.
- Saito, M. (1988), DISPER80: A subroutine package for the calculation of seismic normal-mode solutions, in *Seismological Algorithms*, edited by D. J. Doornbos, pp. 293–319, Elsevier, New York.
- Shen, Y., and D. W. Forsyth (1995), Geochemical constraints on initial and final depths of melting beneath mid-ocean ridges, *J. Geophys. Res.*, *100*(B2), 2211–2237.
- Smith, G. P., D. A. Wiens, K. M. Fisher, L. M. Dorman, S. C. Webb, and J. A. Hildebrand (2001), A complex pattern of mantle flow in the Lau backarc, *Science*, *292*, 713–716.
- Stern, R. J., M. J. Fouch, and S. L. Klemperer (2003), An overview of the Izu-Bonin-Mariana subduction factory, in *Inside the Subduction Factory*, edited by J. M. Eiler, AGU, Washington, D. C.
- Stolper, E., and S. Newman (1994), The role of water in the petrogenesis of Mariana trough magmas, *Earth Planet. Sci. Lett.*, *121*, 293–325.
- Takahashi, N., S. Kodaira, S. L. Klemperer, Y. Tatsumi, Y. Kaneda, and K. Suyehiro (2007), Crustal structure and evolution of the Mariana intra-oceanic island arc, *Geology*, *35*(3), 203–206.
- Tibi, R., D. A. Wiens, and X. Yuan (2008), Seismic evidence for wide-spread serpentinized forearc mantle along the Mariana convergent margin, *Geophys. Res. Lett.*, *35*, L13303, doi:10.1029/2008GL034163.
- Tolstoy, M., A. J. Harding, and J. A. Orcutt (1993), Crustal thickness on the Mid-Atlantic Ridge: Bull's-eye gravity anomalies and focused accretion, *Science*, *262*, 726–729.
- Volpi, T., A. Gorbatov, H. Shiobara, H. Sugioka, K. Mochizuki, and Y. Kaneda (2006), Shear-wave splitting in the Mariana trough—A relation between back-arc spreading and mantle flow? *Earth Planet. Sci. Lett.*, *244*, 566–575.
- Wagner, L. S., S. Beck, and G. Zandt (2005), Upper mantle structure in the south central Chilean subduction zone (30°–36°S), *J. Geophys. Res.*, *110*, B01308, doi:10.1029/2004JB003238.
- Weeraratne, D. S., D. W. Forsyth, K. M. Fischer, and A. A. Nyblade (2003), Evidence for an upper mantle plume beneath the Tanzanian craton from Rayleigh wave tomography, *J. Geophys. Res.*, *108*(B9), 2427, doi:10.1029/2002JB002273.
- Weeraratne, D. S., D. W. Forsyth, Y. Yang, and S. C. Webb (2007), Rayleigh wave tomography beneath intraplate volcanic ridges in the South Pacific, *J. Geophys. Res.*, *112*, B06303, doi:10.1029/2006JB004403.
- Wiens, D. A., K. A. Kelley, and T. Plank (2006), Mantle temperature variations beneath back-arc spreading centers inferred from seismology, petrology, and bathymetry, *Earth Planet. Sci. Lett.*, *248*, 30–42.
- Wiens, D. A., J. A. Conder, and U. H. Faul (2008), The seismic structure and dynamics of the mantle wedge, *Annu. Rev. Earth Planet. Sci.*, *36*, 421–455.
- Xie, J. (1992), Shear-wave splitting near Guam, *Phys. Earth Planet. Inter.*, *72*, 211–219.
- Yang, Y., and D. W. Forsyth (2006a), Rayleigh wave phase velocities, small-scale convection, and azimuthal anisotropy beneath southern California, *J. Geophys. Res.*, *111*, B07306, doi:10.1029/2005JB004180.
- Yang, Y., and D. W. Forsyth (2006b), Regional tomographic inversion of the amplitude and phase of Rayleigh waves with 2-D sensitivity kernels, *Geophys. J. Int.*, *166*, 1148–1160.
- Zhao, D., A. Hasegawa, and H. Kanamori (1994), Deep structure of Japan subduction zone as derived from local, regional, and teleseismic events, *J. Geophys. Res.*, *99*(B11), 22,313–22,329.
- Zhao, D., Y. Xu, D. A. Wiens, L. M. Dorman, J. Hildebrand, and S. C. Webb (1997), Depth extent of the Lau back-arc spreading center and its relation to subduction processes, *Science*, *278*(5336), 254–257.
- Zhou, Y., F. A. Dahlen, and G. Nolet (2004), Three-dimensional sensitivity kernels for surface wave observables, *Geophys. J. Int.*, *158*, 142–168.

M. L. Pyle, Department of Geology and Geophysics, University of Utah, Salt Lake City, UT 84112, USA. (moira.pyle@utah.edu)

H. Shiobara, Earthquake Research Institute, University of Tokyo, 1-1-1 Yayoi, Bunkyo-ku, Tokyo 113-0032, Japan. (shio@eri.u-tokyo.ac.jp)

P. J. Shore and D. A. Wiens, Department of Earth and Planetary Sciences, Washington University in St. Louis, St. Louis, MO 63130, USA. (patrick@seismo.wustl.edu; doug@wustl.edu)

H. Sugioka, IFREE, JAMSTEC, 2-15 Natsushima-Cho, Yokosuka 237-0061, Japan. (hikari@jamstec.go.jp)

D. S. Weeraratne, Department of Geological Sciences, California State University, Northridge, CA 91330, USA. (dsw@csun.edu)